Egypt. J. Chem. **Vol. 65**, No. 11 pp. 431 - 446 (2022)

Egyptian Journal of Chemistry

http://ejchem.journals.ekb.eg/

Sol–gel synthesis, structure, ferromagnetism and optical properties of Mn–doped titania diluted magnetic semiconductors nanoparticles

Gehad A. M. Alorabi [1,*], S. M. Abdelwahab [2], S. M. Abo-Naf [1]

[1] *Glass Research Department, National Research Centre (NRC), El-Buhouth St., Dokki, 12622 Cairo, Egypt*
[2] *Chemistry Department, Faculty of Science, Ain-Shams University, Cairo, Egypt*

Abstract

Diluted magnetic semiconductors composed of $Ti_{1-x}Mn_xO_2$ nanoparticles, where *x* ranges from 0.0 to 0.1, were synthesized utilizing the sol–gel processing. X-ray diffraction (XRD), high resolution transmission electron microscopy, ultraviolet–visible (UV–Vis) diffuse reflectance spectroscopy (DRS) and vibrating sample magnetometry (VSM) were used for structural, optical and magnetic characterization of the prepared nanomaterials. XRD revealed the coexistence of nanosized anatase and rutile phases with no secondary phase up to $x = 0.07$. When $x = 0.1$, a minority of secondary Mn_2O_3 phase was detected. It was also found that increasing *x*, i.e. increase of Mn content, increased the anatase content at the expense of rutile, increased the cell parameters of both of anatase and rutile, and decreased the average crystallite nanosize of both of them. UV–Vis DRS absorption spectra exhibited peaks around 415–435 and 515 nm which corresponded to Mn^{2+} and Mn^{3+} ions, respectively. The band gap (E_{opt}) values suggest the semiconducting behavior for all the investigated compositions. E_{opt} significantly decreased with increasing Mn concentration. VSM results indicated that pure titania is diamagnetic. While, all the studied Mn-doped TiO_2 compositions exhibited room temperature ferromagnetism. However, weaker ferromagnetism, shown by increased unsaturation, was observed with increasing Mn content.

Keywords: Sol–gel; TiO_2; Ferromagnetism; Diluted magnetic semiconductors (DMS); Nanoparticles

1. Introduction

Doping of magnetic ions into a semiconductor nanostructured lattice constitutes a category of advanced multifunctional materials known as diluted magnetic semiconductors (DMS). Thus, in DMS, the exchange interaction between delocalized valence- and/or conduction-band charge carriers of the host semiconductor and localized spin of the magnetic dopant brings about generation of new beneficial spin-based electronic and optical properties. The charge carriers are typically s and/or p electrons and/or holes, while the magnetic ions participate with d-electrons and, hence, these interactions are termed as sp–d exchange interactions [1]. Recently, DMS have attracted tremendous interest in fundamental research and potential applications in magneto-electronic, magneto-optic and spintronic devices [2−5]. The key requirement for the realization of spintronic devices is the development of ferromagnetic DMS with Curie temperature (T_C) at or above room temperature [2]. Nowadays, huge interest is directed to DMS based on TiO_2, ZnO and SnO_2 doped with transition metal (TM) ions such as Fe, Co, Mn, Ni, Cr, Cu, V and etc. [6−10]. Among these oxide semiconductors, nanosized TiO_2 matrix is a promising candidate for application as DMS due to numerous advantages such as the easily modifiable electronic, magnetic, phonon and optical properties via doping with TM ions, wide band-gap semiconductor (band gap is 3.02 eV for rutile and 3.23 eV for anatase), high n–type carrier mobility and outstanding stability relative to other DMS oxides [11−13]. Development of spintronic and optoelectronic devices is particularly

*Corresponding author e-mail: ga302056@gmail.com; (Gehad A. M. Alorabi).
Receive Date: 23 June 2022; Revise Date: 07 July 2022; Accept Date: 12 July 2022.
DOI: 10.21608/ejchem.2022.145177.6369.

dependent on formation of nanostructured materials because of their attractive properties compared with the counterpart bulk materials [14]. Moreover, TiO_2 nanoparticles contain a large number of surface oxygen vacancies, due to both quantum size and surface effects, which intensively influence the electronic states and, consequently, improve the optical and magnetic features [15]. TiO_2 has three polymorphs which are anatase, rutile and brookite. This variety in crystal structure promotes widely varied chemical and physical properties which gives rise to variable performance in different practical applications. Anatase is a stable phase in photocatalysis applications. Rutile is a high temperature stable phase. Brookite has the least stability in comparison to anatase and rutile [16]. In many cases, properties of TiO_2 matrices can be tailored via adapting crystal structure composed of a mix of anatase and rutile. Providing these characteristics, titania has been comprehensively explored as a convenient material of choice also in other technological applications such as photocatalysis, transparent conductive coatings, photovoltaics, sensors, solar cells, data storage devices, organic light emitting diodes (OLED) and UV light absorber [16, 17].

As a dopant, manganese has different valence states which are Mn^{2+}, Mn^{3+}, Mn^{4+}, Mn^{6+} and Mn^{7+}; and their coexistence promotes appearance of different energy levels at variable Mn concentrations. This narrows the band gap at different levels which, in turn, can effectively alter the semiconducting and magnetic properties giving rise to a beneficial impact in the resulting doped materials [18]. Considering the preparation, there are several methods such as hydrothermal, precipitation, micro-emulsion, electrochemical and solid-state reactions as well as sol–gel processing. In the present study, sol–gel method was selected as it is characterized by low temperature processing, low cost and more control on the purity, homogeneity and chemical composition of the products. Furthermore, very small contents of doping elements can be introduced into the sol and occurs finely and homogeneously dispersed in the final material exhibiting very efficiently the desired property [19].

In the current work, the sol-gel method was utilized for synthesis of $Ti_{1-x}Mn_xO_2$ nanopowders with $0 \le x \le 0.1$. It is aimed, then, to investigate the structure, morphology, optical and magnetic properties of these Mn-doped titania nanoparticles by different analytical tools.

Table 1
Chemical composition, abbreviations and E_{opt} of the sol-gel synthesized $Ti_{1-x}Mn_xO_2$ nanoparticles

Sample code	Chemical composition (at.%)	E_{opt} (eV) ± 0.005
100Ti	Pure titania	3.132
0.5Mn	$Ti_{0.995}Mn_{0.005}O_2$	2.262
1Mn	$Ti_{0.99}Mn_{0.01}O_2$	2.188
1.5Mn	$Ti_{0.985}Mn_{0.015}O_2$	1.835
3Mn	$Ti_{0.97}Mn_{0.03}O_2$	1.617
5Mn	$Ti_{0.95}Mn_{0.05}O_2$	1.463
7Mn	$Ti_{0.93}Mn_{0.07}O_2$	1.436
10Mn	$Ti_{0.9}Mn_{0.1}O_2$	1.382

2. Materials and methods

2.1. Materials

Analytical reagent grade chemicals were used in the current sol–gel synthesis. These are: both of titanium(IV) n-butoxide, $C_{16}H_{36}O_4Ti$ or specifically ($Ti[O(CH_2)_3CH_3]_4$), colorless liquid 99+%; and ethyl acetoacetate, $C_6H_{10}O_3$, colorless liquid 99+%, were purchased from Alfa Aesar, Germany. Absolute ethanol (C_2H_5OH, EtOH), 99+% extra pure was purchased from Fisher Scientific, UK. Hydrochloric acid (HCl), 37% certified AR for analysis was purchased from Roth Chemie GmbH, Germany. Manganese(II) acetate anhydrous ($Mn(CH_3COO)_2$, $Mn(ac)_2$), +98% was purchased from Acros organics. Ethylene glycol ($C_2H_6O_2$, EG), +99% extra pure was purchased from SDF, India.

2.2. Sol–gel synthesis process

Eight Mn-doped titania, having the chemical compositions of $Ti_{1-x}Mn_xO_2$ where $0 \le x \le 0.1$ as indicated in Table 1, were synthesized by the sol–gel method. Specifically, x= 0.0, 0.005, 0.01, 0.015, 0.03, 0.05, 0.07 and 0.1. Pure titania with x= 0.0 was

prepared as blank reference material to which the Mn-doped compositions will be compared. In the employed sol–gel route, titanium n-butoxide (Ti(O-Bu^n)$_4$) was used as the precursor for preparation of titania sol through acid-catalyzed hydrolysis at room temperature using absolute EtOH and HCl as solvent and catalyst, respectively. In order to avoid fast hydrolysis and precipitation of titanium hydroxide, Ti(O-Bu^n)$_4$ was firstly chelated by ethyl acetoacetate (Et-Ac-Ac). The molar ratio of Ti(O-Bu^n)$_4$ to Et-Ac-Ac was 1:2. Mixing of these two colorless liquids yielded clear transparent yellow complex solution to which the EtOH and distilled H_2O were added under continuous stirring at room temperature (RT). The molar ratio of Ti:H_2O:EtOH was 1:2:20, respectively. Then, 1M HCl was added until the acidic condition of solution was adjusted at pH= 2 producing a stable transparent yellow titania sol. In case of Mn-doped TiO_2 compositions, the appropriate amount of $Mn(ac)_2$ was dissolved in EG for 1 h at RT adapting a molar ratio of $Mn(ac)_2$:EG equals to 1:20. This Mn-containing solution was added to the titania sol and kept stirred at RT for 1 h. Warming of sols containing different Mn concentrations at 55-60 °C for 30 min led to the formation of transparent gels. In order to obtain the pure TiO_2 and Mn-doped TiO_2 nano-powders, the formed gels were successively dried at 95, 120 and 200 °C, each for 4 h. The alcohols used as solvent and produced, in the course of current sol-gel reactions, as bi-product are ethanol and n-butanol, respectively, whose evaporation temperatures are 78 and 118 °C, respectively. Also, Et-Ac-Ac and EG are evaporated at 180 and 197 °C, respectively. Therefore, drying at 200 °C was carried out in order to evaporate all these organic solvents and chelating agents. Then, the dry powder was subjected to a heat-treatment up to 550 °C using a heating rate of 1 °C/min followed by keeping at 550 °C for 4 h. Samples codes, which indicate the Mn concentration, were used for brief identification of compositions of the prepared materials and are given in Table 1.

2.3. Characterization

The identity of crystalline phases of synthesized materials was identified by means of powder X-ray diffraction (XRD) analysis using an EMPYREAN PanAlytical x'pert PRO MRD diffractometer equipped with a Ni-filtered Cu-K_α X-ray radiation source (λ= 1.5406 Å) powered at 45 kV and 30 mA. Diffractograms were recorded in the 2θ range from 4º to 80º. The employed phases identification software was high score plus. High resolution transmission electron microscopy (HRTEM) was utilized to study the morphology of the synthesized pure TiO_2 as well as Mn-doped TiO_2 using a JEOL JEM-2100 (Japan) microscope operated at accelerating voltage of 200 kV with a resolution of 1.402 Å. Lattice interlayer d-spacing was investigated by recording the inverse fast Fourier transformation (IFFT) profiles. Optical properties of synthesized materials were studied by measuring the ultraviolet-visible (UV-Vis) optical absorbance and diffuse reflectance spectra (DRS), in the wavelength range of 200-1000 nm, applying the Kubelka-Munk function for determination of the band gap energy (E_{opt}) using a spectrophotometer type T80 PG Instruments, England. Room temperature magnetization (M) and magnetic hysteresis (M-H) loops of the synthesized materials were measured using vibrating sample magnetometer (VSM; LakeShore 7410, USA) under applied magnetic field between –10 and 10 kOe.

3. Results and discussion

3.1. Structural XRD results

XRD patterns of the pure TiO_2 and Mn-doped TiO_2 with different Mn concentrations are shown in Figs. 1 and 2. The reference intensity ratio (RIR) calculations were performed in XRD analysis in order to correlate quantitatively the percentage of constituting phases with the Mn content. The obtained XRD results are mentioned in detail in Table 2. The recorded diffraction peaks demonstrated formation of two phases. The main phase was tetragonal anatase nanocrystalline TiO_2 which agrees with the ICSD reference code 98-015-4603 with space group $I4_1/amd$ and space group No. 141 whose standard lattice constants a=b= 3.7850 Å and c= 9.4820 Å [20, 21]. The second phase was tetragonal rutile TiO_2 that is indexed to the ICSD code 98-005-

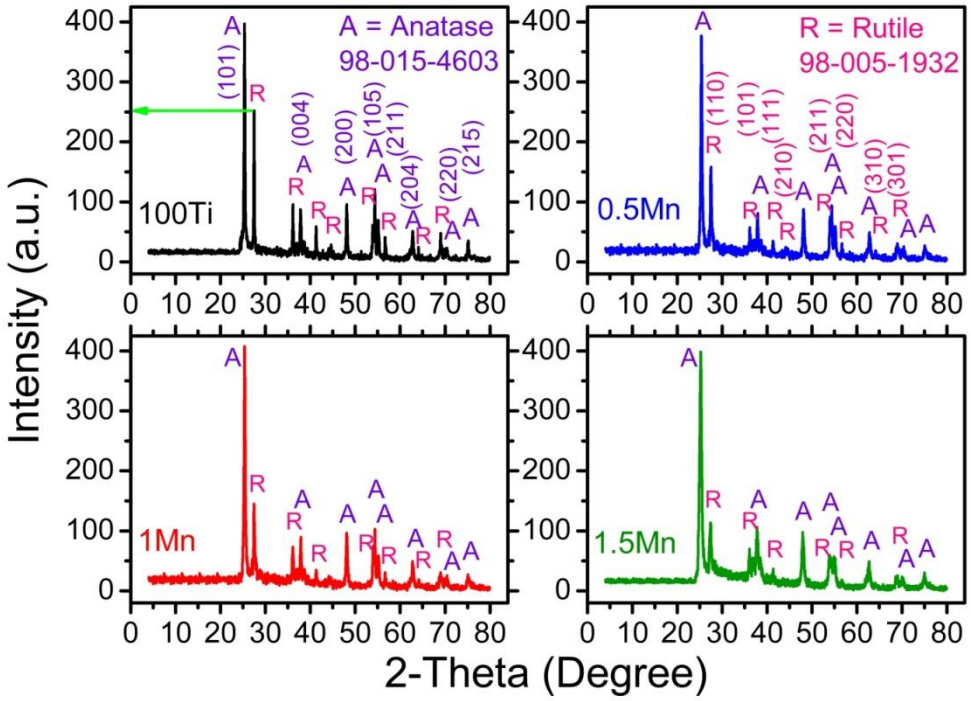

Fig. 1. X-ray diffraction patterns of the synthesized $Ti_{1-x}Mn_xO_2$ nanocrystalline powders, with x= 0.0, 0.005, 0.01 and 0.015, after 550 °C.

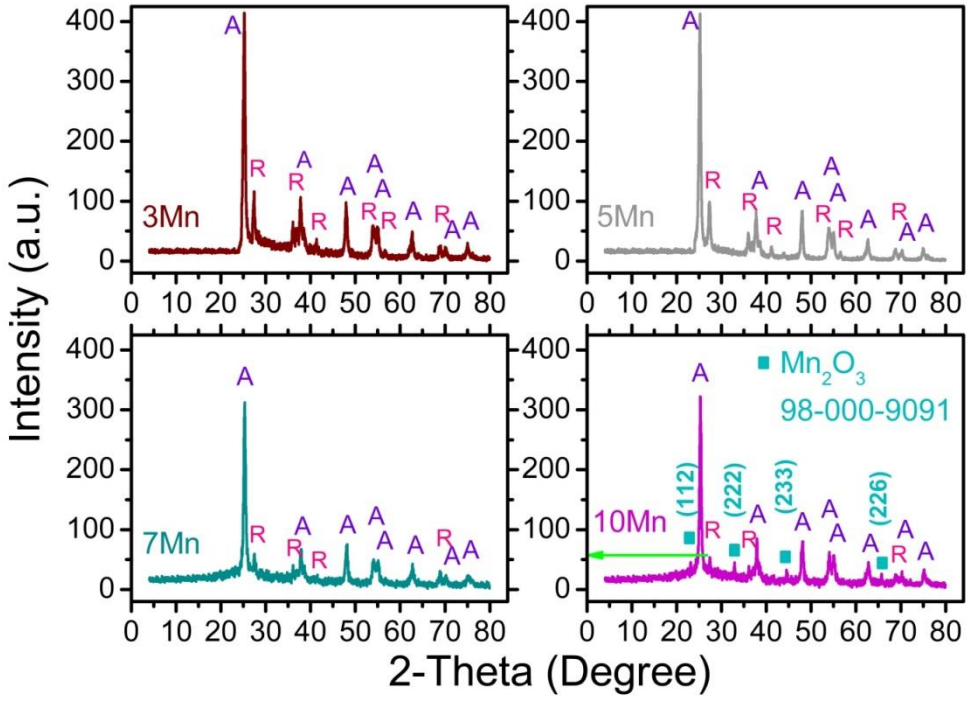

Fig. 2. X-ray diffraction patterns of the $Ti_{1-x}Mn_xO_2$ nanopowders, with x= 0.03, 0.05, 0.07 and 0.1, after 550 °C.

1932 with space group $P4_2/mnm$ and space group No. 136 whose standard lattice constants a=b= 4.5980 Å and c= 2.9560 Å. The main peaks of anatase were recorded at 2θ= 25.32°, 37.93°, 48.04° and 54.04° which corresponded to Bragg reflection planes of (101), (004), (200) and (105), respectively. The main peaks of rutile were recorded at 2θ= 27.41°, 36.09°, 41.24° and 54.30° which corresponded to reflection planes of (110), (101), (111) and (211), respectively [22]. Up to 7 at.% of Mn, no Mn secondary phase was detected. This means that this content of Mn cations successfully substituted Ti^{4+} in the TiO_2 network warranting the absence of metallic clusters or Mn oxides. Only when *x*= 0.1, i.e. 10 at.% of Mn, a minority of 5.3% of Mn_2O_3 phase was crystallized. This phase was identified to be a cubic Bixbyite C matched with the ICSD code 98-000-9091 with space group Ia–3 and space group No. 206 whose standard lattice constants a=b=c= 9.4150 Å. The main peaks of this Mn_2O_3 phase were located at 2θ= 23.12°, 32.93°, 45.13° and 65.74° which corresponded to (112), (222), (233) and (226) reflection planes, respectively [23].

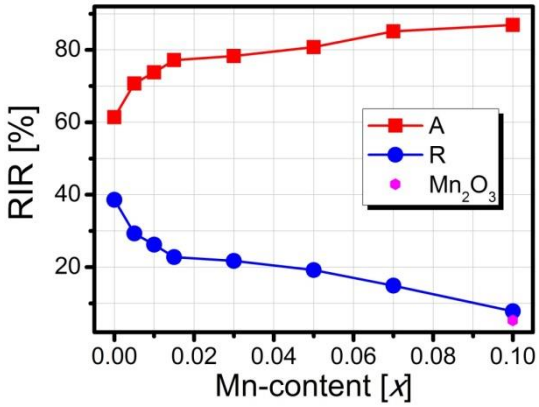

Fig. 3. RIR presenting the variation of phase ratio of anatase, rutile and Mn_2O_3 phases with change of Mn-content in the synthesized $Ti_{1-x}Mn_xO_2$ nanoparticles.

The pure titania, sample 100Ti, contains 61.4% anatase and 38.6% rutile. Introduction of manganese and increase of its concentration monotonically enhanced the formation of anatase, i.e. increased the percentage of anatase and reduced that of rutile, such that anatase reached 86.9% while rutile was diminished to 7.8% in the sample containing the highest Mn content, i.e. *x*= 0.1 (sample 10Mn). This can be obviously seen by the green arrow comparing intensity of the most intense peak of rutile in these two compositions as illustrated in Figs. 1 and 2. The gradual change of contents of anatase and rutile in the synthesized materials as a function of Mn content is graphically represented in Fig. 3.

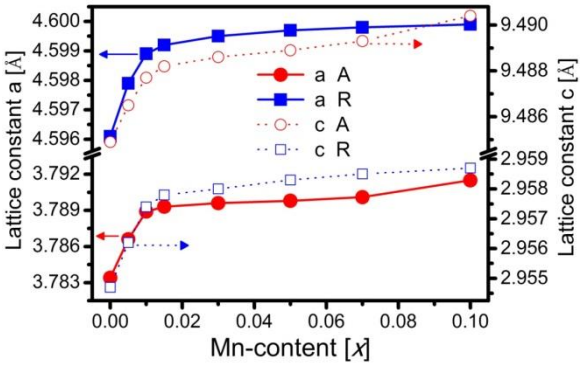

Fig. 4. Variation of lattice constants "a" and "c" of anatase and rutile phases with change of Mn-concentration in the prepared $Ti_{1-x}Mn_xO_2$ nanoparticles.

The variation of lattice constants ("a" and "c") as well as unit cell volume (V) of anatase and rutile phases with increasing Mn-content is also listed in Table 2 and is graphically shown in Fig. 4. These lattice parameters showed firstly, in cases of *x*= 0.005 and 0.01, noticeable increase (which means lattice unit expansion) and, then, only slight increase can be observed. In order to understand this change, the ionic radii of Ti^{4+} and Mn cations; i.e. mostly Mn^{2+}, Mn^{3+} and Mn^{4+}; have to be considered. These are: Ti^{4+}= 0.61 Å, Mn^{2+}= 0.82 Å, Mn^{3+}= 0.58 Å and Mn^{4+}= 0.53 Å, all for the six-fold coordination [3, 24–28]. The radii of Mn cations are evidently dependent on the valence state. From the current XRD results, no sign for the presence of Mn^{4+}, i.e. no MnO_2 phase, was detected. Even Mn^{4+} ions present without crystallization, the lattice parameters would be expected to decrease, i.e. lattice unit contraction would occur [26]. However, Mn^{3+} could only be detected as Mn_2O_3 in case of *x*= 0.1. Therefore, it can be pointed out that the lattice unit expansion is mainly due to the larger Mn^{2+} ions which were successfully incorporated into the titania lattice crystallographic structure at the Ti^{4+} sites [3, 24, 25]. The slight increase observed thereafter is reasonably attributed to the coexistence of Mn^{2+} and Mn^{3+} ions.

This is further supported by the optical absorption measurement mentioned in section 3.3.

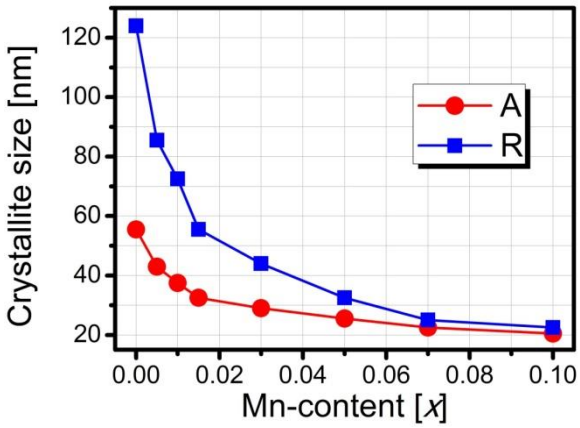

Fig. 5. Variation of average crystallite size, calculated from Scherrer's equation, of the anatase and rutile phases with Mn-doping.

The average crystallite sizes (D), of both of anatase and rutile phases, were calculated from full width at half maximum of the most intense peak of each phase using Scherrer's formula [18, 25], i.e. peak corresponding to (101) crystal plane for anatase and that to (110) for rutile. The crystallite size (D) can be calculated from Scherrer's equation as following:

$$D = 0.9\,\lambda\ /\ (\beta\cos\theta)$$

where λ is the employed X-ray wavelength (λ= 1.5406 Å), θ is the Bragg angle of the corresponding peak, β is the full width at half maxima (FWHM). These calculations confirmed the formation of TiO_2 lattice composed of nanosized anatase and rutile. The obtained sizes are listed in Table 2 and plotted as a function of Mn concentration (*x*) in Fig. 5. It is clearly seen that increasing *x* resulted in decrease of the nanosize of both phases. For anatase, D decreased from 55.5 to 20.5 nm. For rutile D decreased from 124 to 22.5 nm. Analogous observation of the influence of Mn-doping on crystallite nanosize of TiO_2 matrices was also found in previous articles [18, 24, 25, 28, 29]. This reduction in the crystallite sizes might be attributed to the lattice distortion caused by the difference in ionic radii of Mn cations (herein Mn^{2+} and Mn^{3+}) and Ti^{4+} ions which limits the growth rate [18, 25, 28, 29].

3.2. Morphological HRTEM analysis

Systematic morphological HRTEM analysis was performed in order to study the shape and size of synthesized nanoparticles as well as to support the obtained XRD results by recording the IFFT profiles for lattice d-spacing investigation, as possible as we could. Low magnification TEM images of the pure and Mn-doped TiO_2 are given in Fig. 6a,c,e; Fig. 7a,c,e and Fig. 8a,d. These micrographs indicated that the nanoparticles were apparently agglomerated with different granular shapes and sizes. A decrease in the nanosize can be clearly noticed with increasing Mn content which agreed with the results obtained from XRD analysis. The presence of rutile phase, in samples 100Ti and 0.5Mn, was further confirmed and visualized by obtaining the lattice fringes and IFFT profiles, displayed in Fig. 6b,d, which indicate d-spacings of 0.3215 and 0.3213 nm, respectively, corresponding to the (110) crystal plane of rutile [30]. Fig. 6f depicts the lattice fringes of sample 1Mn which contain two d-spacing values of 0.35 and 0.25 nm in crystallites having sizes of 6.8 and 4.5 nm, respectively, corresponding to the (101) and (101) crystal planes of anatase and rutile phases, respectively [25, 30−34]. Similarly, in Figs. 7b,f and 8b, well-resolved lattice fringes, indicating d-spacing of 0.35 nm corresponding to the (101) crystal plane of anatase, were obtained in cases of samples 1.5Mn, 5Mn and 7Mn. Figs. 7f and 8b show crystallites having sizes of 9.5 and 21.24 nm, respectively. Whereas, Fig. 7d shows the HRTEM lattice image of sample 3Mn which indicated d-spacing of 0.18 nm corresponding to the (200) crystal plane of anatase [32]. In case of sample 10Mn which contains 5.3% nanocrystals of Mn_2O_3, a very well-resolved HRTEM image was obtained and it is depicted in Fig. 8c. This image showed periodic lattice fringes, with obvious line-shape structure, indicating d-spacing of 0.28 nm corresponding to the (222) crystal plane of Mn_2O_3 [35]. This interplanar spacing was further confirmed by recording the IFFT profile for the same zone in this image which revealed a value of 0.2818 nm that is also given in Fig. 8c.

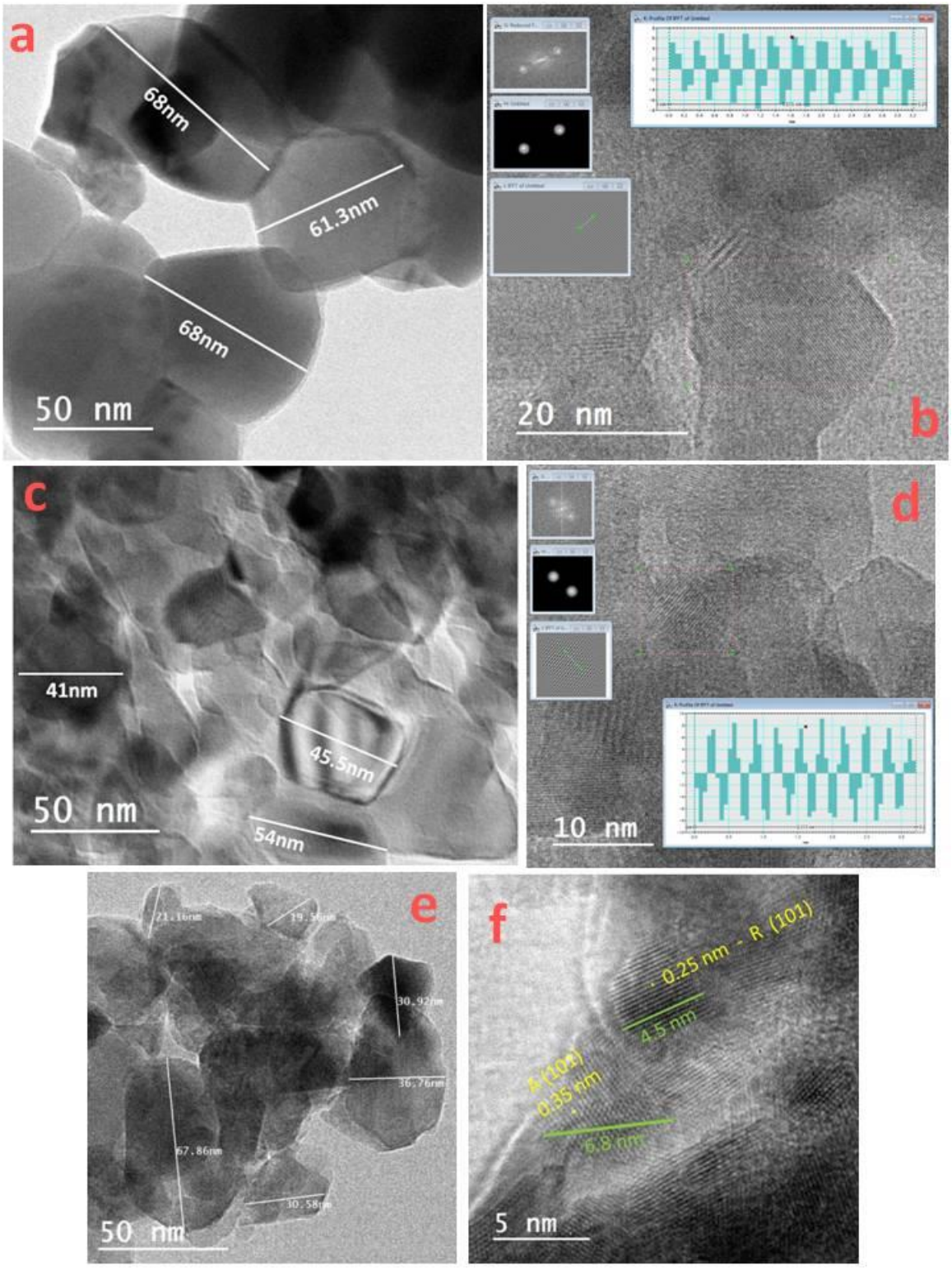

Fig. 6. HRTEM images of samples: a) pure titania (100Ti), b) its IFFT profile, c) 0.5Mn, d) its IFFT profile, e) 1Mn and f) its high magnification (HM) image showing interplanar d-spacings of anatase and rutile.

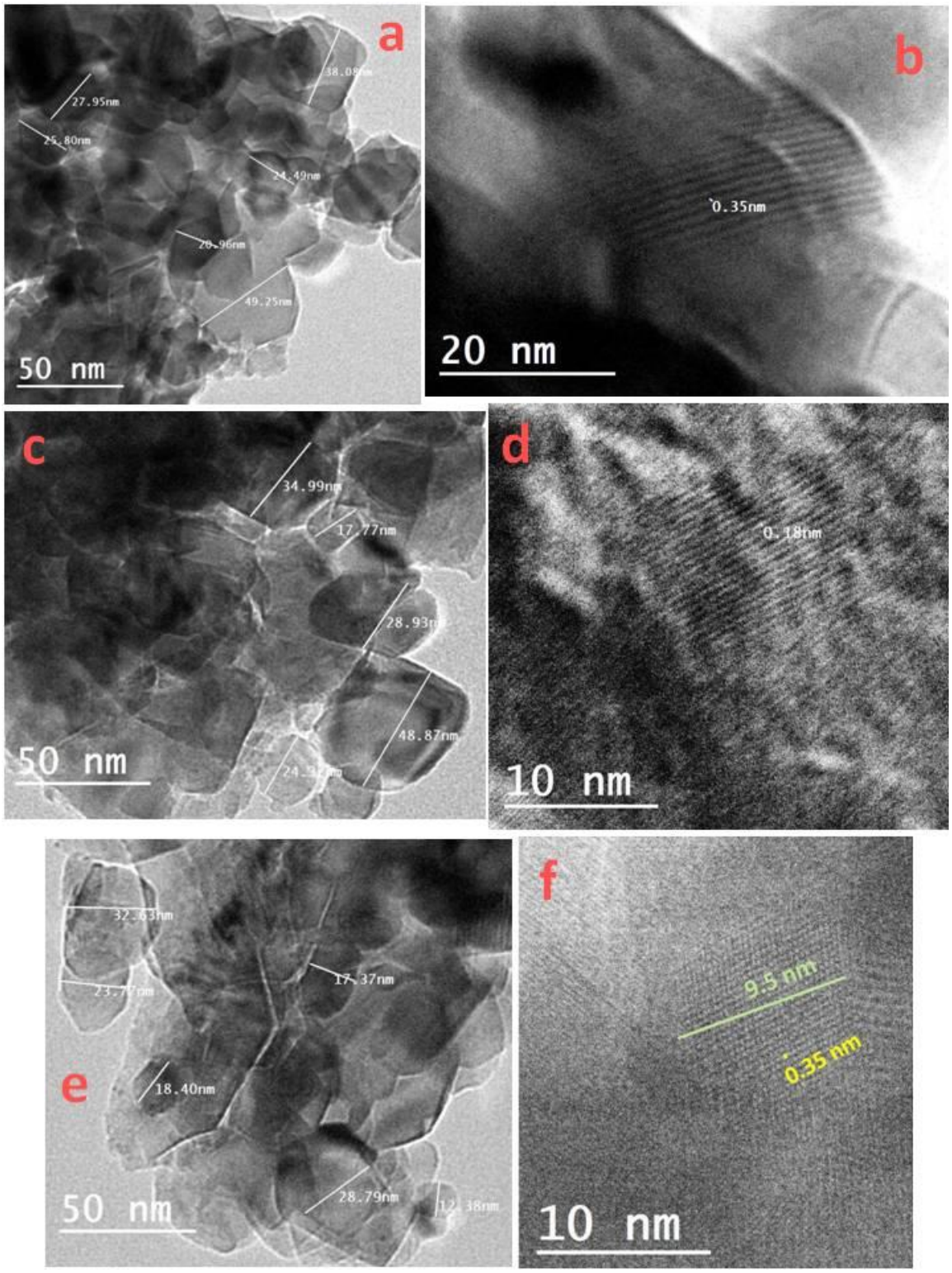

Fig. 7. HRTEM images of samples: a) 1.5Mn, c) 3Mn, e) 5Mn and (b,d,f) their HM images, respectively, showing interplanar d-spacings of anatase.

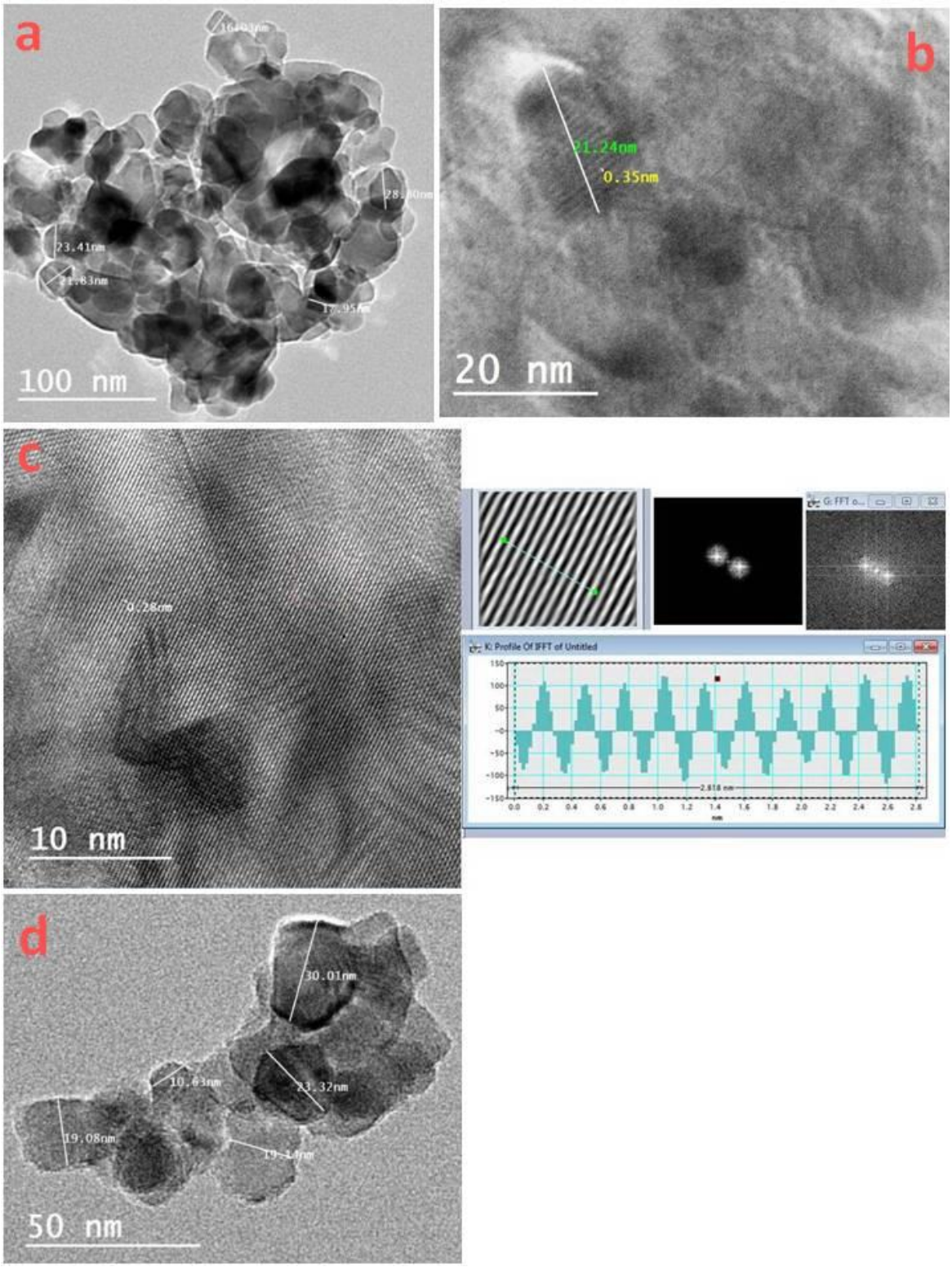

Fig. 8. a) TEM image of sample 7Mn, b) its HM image showing interplanar d-spacing of anatase, c) HR lattice image of Mn_2O_3 crystallized in sample 10Mn with the corresponding IFFT profile and d) TEM image of sample 10Mn as a whole.

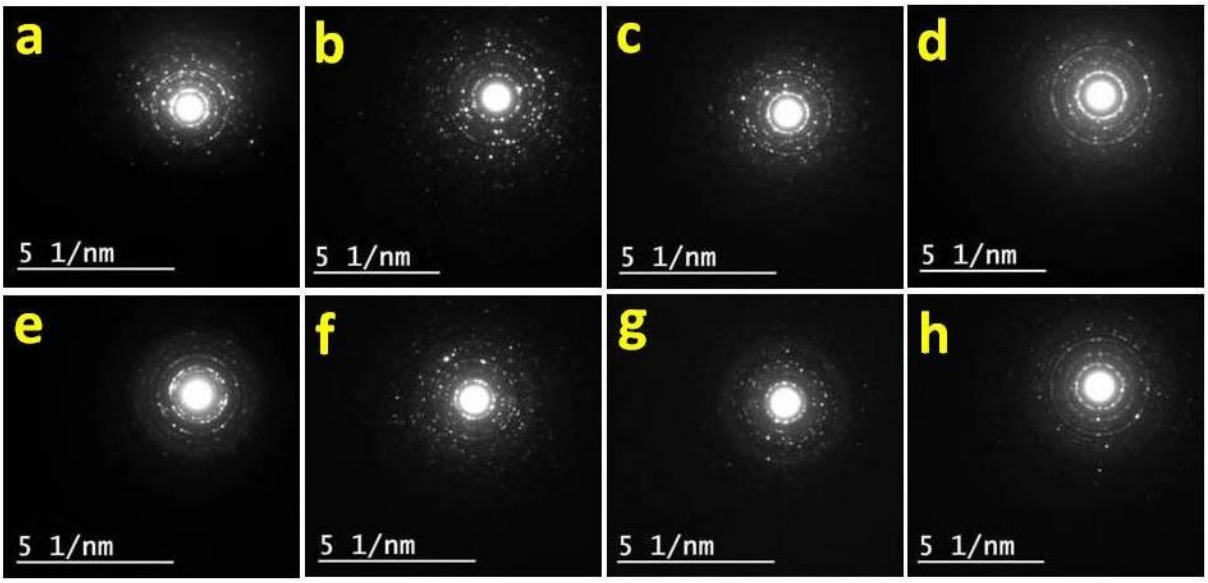

Fig. 9. (a–h) SAED patterns of the synthesized $Ti_{1-x}Mn_xO_2$ nanoparticles with x= 0.0–0.1, respectively.

Table 2

Variation of anatase and rutile phases ratio, their lattice constants ("a" and "c"), unit cell volume (V) and average crystallite size (D) with Mn-content; calculated from XRD analysis

Sample code	Phases	Phase ratio (%)	a (Å)	c (Å)	V ($Å^3$)	D (nm)
100Ti	A	61.4	3.7834	9.4849	135.768	55.5
	R	38.6	4.5961	2.9547	62.415	124
0.5Mn	A	70.7	3.7866	9.4865	136.021	43
	R	29.3	4.5979	2.9562	62.496	85.5
1Mn	A	73.8	3.7889	9.4877	136.203	37.5
	R	26.2	4.5989	2.9574	62.549	72.5
1.5Mn	A	77.2	3.7893	9.4882	136.239	32.5
	R	22.8	4.5992	2.9578	62.565	55.5
3Mn	A	78.3	3.7896	9.4886	136.266	29
	R	21.7	4.5995	2.9580	62.578	44
5Mn	A	80.8	3.7898	9.4889	136.285	25.5
	R	19.2	4.5997	2.9583	62.589	32.5
7Mn	A	85.1	3.7901	9.4893	136.312	22.5
	R	14.9	4.5998	2.9585	62.596	25
10Mn	A	86.9	3.7915	9.4904	136.429	20.5
	R	7.8	4.5999	2.9587	62.603	22.5
	Mn_2O_3	5.3	--	--	--	11.5

A= Anatase, R= Rutile

Selected area electron diffraction (SAED) patterns of all the studied nanoparticles are shown in Fig. 9 which revealed their polycrystalline structure where the characteristic rings distinctly appeared. Inspection of these SAED patterns indicated also the decrease of average crystallite size with increasing Mn-doping concentration (*x*).

3.3. Optical properties

Fig. 10 shows the UV−Vis absorption spectra, derived from DRS, of the studied nanoparticles. This derivation and the corresponding calculation, using Kubelka-Munk function, can be found in detail in previous publications [36, 37]. All the undoped and Mn-doped titania nanoparticles exhibited a broad UV peak centered at 245 nm. Pure titania exhibited no other visible bands with an absorption edge around 325 nm. The structure of TiO_2 lattice is built via the hybridization between the 2p orbitals of oxygen and 3d orbitals of titanium. TiO_2 is an intrinsic wide-band gap semiconductor and, hence, results in no visible absorption [38, 39]. The UV band at 245 nm was ascribed to the intrinsic band-gap absorption of titanate matrix, i.e. electronic transition from the valence band (VB) to conduction band (CB) [34, 39, 40]. Mn-doped TiO_2 matrices with x= 0.005 and 0.01 showed additional visible band centered at 415 nm, and the absorption edge was shifted to about 480-500 nm. In case of x= 0.015 and 0.03, this band was shifted to 435 nm with the appearance of broad shoulder around 515 nm. For the Mn-doping concentrations of x= 0.05, 0.07 and 0.1, their spectra showed a very broad intense visible band consisting of two heads at about 435 and 515 nm. The bands at 415 and 435 nm were assigned to the $^6A_{1g}\rightarrow[^4A_{1g}, {}^4E_g]$ electronic transition of $3d^5$ Mn^{2+} ions [19, 41−43], while the shoulder and the band at 515 nm are attributed to the $^5E_g\rightarrow{}^5T_{2g}$ transition of $3d^4$ Mn^{3+} ions [41, 44]. Therefore, Mn was initially incorporated in the TiO_2 lattice solely as Mn^{2+} ions which accounted for the noticeable increase of lattice constants, determined from the XRD analysis, in cases of x= 0.005 and 0.01. Successive increase of the Mn-doping concentration resulted in gradual participation of Mn^{3+} ions until nearly balanced proportion of both of Mn^{2+} and Mn^{3+} ions coexist which accounts for the very slight increase of lattice constants thereafter. It can be obviously noticed that the absorption edge was monotonically shifted to longer wavelength, i.e. red shift, as x increases. This is logically related to the change in optical band gap energy (E_{opt}) with Mn-doping.

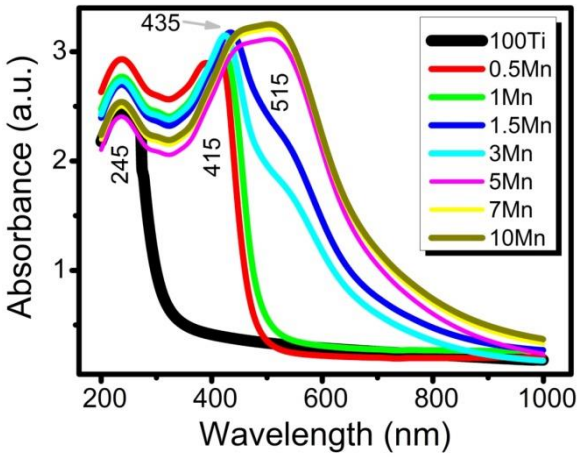

Fig. 10. UV–Vis absorption spectra of the investigated $Ti_{1-x}Mn_xO_2$ nanoparticles.

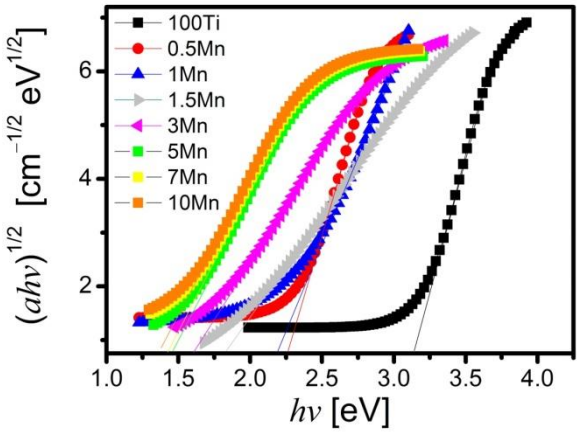

Fig. 11. Tauc plots of $(\alpha hv)^{1/2}$ vs. photon energy (hv) of the investigated $Ti_{1-x}Mn_xO_2$ nanoparticles.

Knowing that TiO_2 lattice has an indirect band gap transition [25, 40, 45], E_{opt} of the studied $Ti_{1-x}Mn_xO_2$ nanoparticles was determined from Tauc plot of $(\alpha hv)^{1/2}$ versus photon energy (hv), applying the Kubelka-Munk function, as illustrated in Fig. 11. Details of these calculations are mentioned in Ref. [25]. The obtained E_{opt} values are listed in Table 1. It is evident that E_{opt} showed monotonic decrease with increasing Mn content. For the synthesized pure titania, E_{opt} is 3.132 eV which lied in between those of pure anatase and rutile. This value was decreased to 1.382 eV in case of x= 0.1. This means that

incorporation of Mn cations into the TiO_2 nanolattice resulted in band gap narrowing. Recently, Mn-doping into titanate matrix also resulted in a reduction of the band gap from 3.14 eV to 1.7 eV [46]. Generally, this change can be understood in terms of the evolution of new multiple energy states into the mid band gap region of Mn^{2+}–Mn^{3+}–TiO_2 nanoparticles [25, 46]. Actually, oxygen vacancies (V_O), as defect sites, play another important role in such reduction of the band gap. The trapped electrons in V_O generate donor states near the VB. Increase of V_O concentration gives rise to a positive correction of the VB edge which, consequently, results in shrinkage of the band gap [34, 46]. Moreover, in Mn-doped titania, Ti–O–Mn bonds could also be formed generating another type of defect sites which create more energy states within the band gap and, thus, contributing to the band gap narrowing too [45]. Difference in the ionic radii of Ti^{4+}, Mn^{2+} and Mn^{3+} might also be another cause for the energy gap narrowing [45].

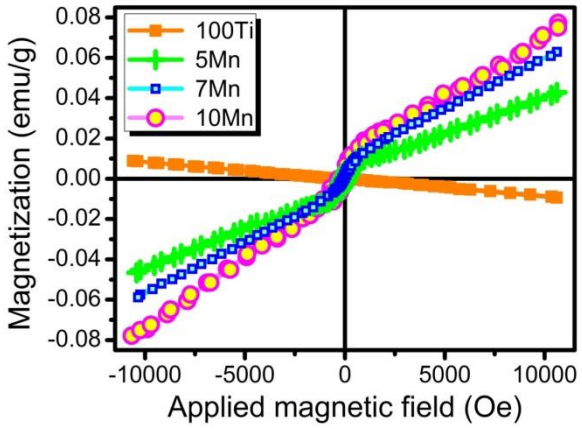

Fig. 12. Room temperature magnetic hysteresis loops of pure titania (100Ti), 5Mn, 7Mn and 10Mn samples.

3.4. Magnetic properties

Figs. 12 and 13 show the room temperature (RT) magnetic hysteresis loops of the studied undoped and Mn-doped titania nanoparticles. The measured magnetization parameters, i.e. magnetization, coercivity and retentivity, are listed in Table 3. As indicated in Fig. 12, pure titania exhibited typical diamagnetic behavior, i.e. linear magnetization with a negative slope. This agrees with several previous published articles [13, 15, 26, 47, 48, 49]. All the Mn-doped TiO_2 compositions exhibited RT ferromagnetic behavior with varied degrees of unsaturation. Therefore, transition from diamagnetism to ferromagnetism demonstrates that the observed ferromagnetic behavior was caused by Mn-doping and was not an intrinsic property of the current synthesized TiO_2 nanolattice. It can be noted that both of the magnetization value and unsaturation increased with increasing Mn concentration. Titania matrices containing low Mn contents, i.e. samples 0.5Mn, 1Mn, 1.5Mn and 3Mn, showed ferromagnetic hysteresis loop with much less unsaturation and relatively low retentivity and coercivity values, as given in Table 3, giving rise to soft ferromagnetic nanomaterials which might be promising DMS for spintronic applications. While, TiO_2 matrices containing higher Mn contents, i.e. samples 5Mn, 7Mn and 10Mn, exhibited weak ferromagnetism with substantial unsaturation due to competing antiferromagnetic and paramagnetic contributions.

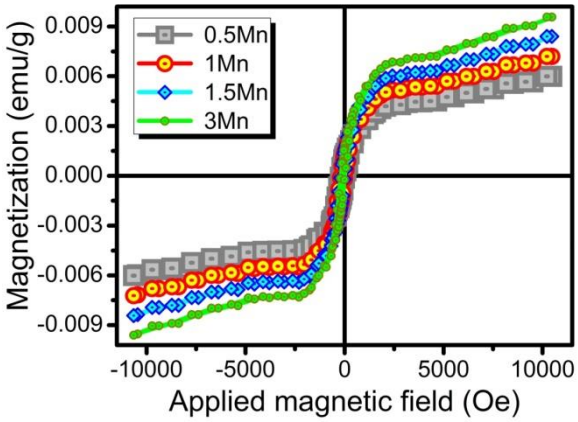

Fig. 13. Room temperature magnetic hysteresis loops of compositions containing relatively lower Mn-content, i.e. 0.5Mn, 1Mn, 1.5Mn and 3Mn samples.

To date, many theoretical concepts can be considered for explanation of the origin of RT ferromagnetism in DMS materials. In the present work, it is convenient to consider the interaction between the dopant and oxygen vacancies (V_O) intrinsically existed in the TiO_2 nanolattice. V_O are necessary to maintain charge neutrality as Mn^{2+} and Mn^{3+} ions substitute for Ti^{4+} in the TiO_2 lattice which was inferred from the optical and XRD analyses. An oxygen vacancy gives one electron to the neighboring

Ti^{4+} sites producing Ti^{3+} ions. As a consequence, Mn^{2+}–V_O–Ti^{3+} and Mn^{3+}–V_O–Ti^{3+} sites with a net magnetic moment were created in the lattice. The magnetic moment, linked with these sites, extends over two or more neighboring Ti sites forming bound magnetic polaron (BMP). According to BMP hypothesis, when V_O defects concentration exceeds the percolation threshold, V_O defects overlap many dopant ions producing a large number of BMPs which bring about the ferromagnetic coupling interaction. Similar interpretations were previously given in cases of ferromagnetic Mg-doped nanostructured TiO_2 [15] and La-Fe-codoped TiO_2 nanoparticles [50]. It may be noted that formation of oxygen vacancies was strongly induced in the synthesized Mn-doped titania lattice owing to the difference in both of the ionic radii and valence states of Mn cations, Mn^{2+} and Mn^{3+}, and Ti^{4+} ions [51, 52]. Greater density of the oxygen vacancies results in a greater overall volume occupied by BMPs and their overlap which enhances long-range ferromagnetic ordering [52]. This occurs under the condition that concentration of the 3d dopant itself, herein Mn^{2+} and Mn^{3+} ions, should be far below the percolation threshold, associated with nearest-neighbor cation coupling, in order to achieve spin-only moment. This interpretation can be fairly applied for explanation of RT ferromagnetism in cases of Mn-doped TiO_2 with low Mn concentrations, namely samples 0.5Mn, 1Mn, 1.5Mn and 3Mn. Higher concentrations of Mn which exceed its percolation threshold; in samples 5Mn, 7Mn and 10Mn; resulted in decrease of the average distance between adjacent Mn ions. This caused the evolution of antiferromagnetic superexchange coupling strength between neighboring Mn ions via nearby O^{2-} ions [52, 53]. Moreover, the increased moments of Mn can create also paramagnetic contribution. In overall, this led to weak ferromagnetism with increased unsaturation in these compositions. Therefore, it can be suggested that both oxygen vacancies and a convenient concentration of Mn cations were essential for achieving ferromagnetism in the current Mn-doped TiO_2 nanoparticles.

4. Conclusions

In conclusion, the effect of Mn-doping on phase structure, ferromagnetism and optical properties of sol–gel synthesized $Ti_{1-x}Mn_xO_2$ nanoparticles has been investigated over a wide range of (x). XRD revealed the coexistence of anatase and rutile in pure TiO_2 in the nanometer size and increase of Mn-doping concentration (x) increased the percentage of anatase and reduced that of rutile. Up to x= 0.07, no secondary phase was detected which confirmed the successful incorporation of Mn cations, Mn^{2+} and Mn^{3+}, into the TiO_2 nanolattice warranting the absence of metallic clusters or Mn oxides. When x= 0.1, only a minority of Mn_2O_3 could be detected. Additionally, increase of x resulted in a monotonic reduction of the crystallite nanosize of both of anatase and rutile. HRTEM and IFFT profiles were employed to investigate the morphology and interplanar d-spacing of the formed nanocrystalline phases. UV–Vis revealed, in agreement with XRD results, the presence of Mn as Mn^{2+} and Mn^{3+} ions. Also, E_{opt} was found to decrease significantly with increasing x. Titania nanoparticles with low x, samples 0.5Mn, 1Mn, 1.5Mn and 3Mn, exhibited RT ferromagnetism and could be promising DMS materials for spintronic applications. This RT ferromagnetic ordering, originating from the interaction between Mn ions and oxygen vacancies, has been explained in terms of the BMP model.

Table 3
Magnetization parameters of the studied $Ti_{1-x}Mn_xO_2$ nanomaterials

Sample code	Magnetization (emu/g) ± 0.2%	Coercivity (G) ± 0.2%	Retentivity (emu/g) ± 0.2%
100Ti	0.0094	2.21	0.000007
0.5Mn	0.0060	112.22	0.000454
1Mn	0.0072	108.74	0.000575
1.5Mn	0.0084	99.62	0.000791
3Mn	0.0096	97.38	0.000895
5Mn	0.0428	82.57	0.000650
7Mn	0.0629	68.48	0.000658
10Mn	0.0774	62.59	0.000675

Acknowledgements

This work was financially supported by the National Research Centre (NRC), Cairo, Egypt; M. Sc. Thesis Fund No. 9/4/11. The authors are thankful and

grateful to NRC-administration for providing this fund.

Declaration of competing interest

The authors declare that they have no known competing financial interests or personal relationships that could have appeared to influence the work reported in this paper.

References

1. Pradhan N., Adhikari S.D., Nag A. and Sarma D.D., Luminescence, plasmonic, and magnetic properties of doped semiconductor nanocrystals. Angew. Chem. Int. Ed. **56**, 7038–7054 (2017).

2. Tian Z.M., Yuan S.L., Yin S.Y., Zhang S.Q., Xie H.Y., Miao J.H., Wang Y.Q., He J.H. and Li J.Q., Synthesis and magnetic properties of vanadium doped anatase TiO_2 nanoparticles. J. Magn. Magn. Mater. **320**, L5–L9 (2008).

3. Kumar A., Kashyap M.K., Sabharwal N., Kumar S., Kumar A., Kumar P. and Asokan K., Structural, optical and weak magnetic properties of Co and Mn codoped TiO_2 nanoparticles. Solid State Sci. **73**, 19–26 (2017).

4. Silveira J.M.D.O., Ubiali A.C.D.L., Baldini D.C., Ciuffi K.J., Rocha L. A. and Nassar E.J., Manganese-doped titania matrix obtained by sol–gel process: Magnetic properties. Microelectron. Eng. **196**, 49–53 (2018).

5. Weissmanna M. and Errico L.A., The role of vacancies, impurities and crystal structure in the magnetic properties of TiO_2. Physica B **398**, 179–183 (2007).

6. Fukumura T. and Kawasaki M. Ferromagnetism in TiO_2- and ZnO-based compounds, functional metal oxides: New science and novel applications, 1st Ed., Edited by Ogale, S. B.; Venkatesan T.V., Blamire M.G., Wiley-VCH Verlag GmbH & Co. KGaA, (2013).

7. Yang S., Jiang D. and Zeng Q., Room temperature ferromagnetism of Fe-doped and (Fe, Cu)-codoped TiO_2 powders prepared by mechanical alloying. J. Mater. Sci. Mater. Electron. **27**, 6570–6577 (2016).

8. Robkhob P., Tang I.M. and Thongmee S., Magnetic properties of the dilute magnetic semiconductor $Zn_{1-x}Co_xO$ nanoparticles., J. Supercond. Nov. Magn. **32**, 3637–3645 (2019).

9. Zhu S., Chen C. and Li Z., Magnetic enhancement and magnetic signal tunability of (Mn, Co) co-doped SnO_2 dilute magnetic semiconductor nanoparticles. J. Magn. Magn. Mater. **471**, 370–380 (2019).

10. Abo-Naf S.M., Ibrahim S. and Marzouk M.A., Structure, optical and ferromagnetic properties of $Zn_{1-x-y}Mn_xCr_yO$ nanoparticles diluted magnetic semiconductors synthesized by citrate sol–gel method. Appl. Phys. A **127**, 404 (2021).

11. Matsumoto Y., Murakami M., Shono T., Hasegawa T.; Fukumura, T., Kawasaki M., Ahmet P., Chikyow T., Koshihara S. and Koinuma H., Room-temperature ferromagnetism in transparent transition metal-doped titanium dioxide. Science **291**, 854–856 (2001).

12. Stella C., Prabhakar D., Prabhu M., Soundararajan N. and Ramachandran K., Oxygen vacancies induced room temperature ferromagnetism and gas sensing properties of Co-doped TiO_2 nanoparticles. J. Mater. Sci. Mater. Electron. **27**, 1636–1644 (2016).

13. Zhang H., Huang W., Lin R., Wang Y., Long B., Hu Q. and Wu, Y., Room temperature ferromagnetism in pristine TiO_2 nanoparticles triggered by singly ionized surface oxygen vacancy induced via calcining in different air pressure. J. Alloys Compd. **860**, 157913 (2021).

14. Quiroz H.P., Serrano J.E. and Dussan A., Magnetic behavior and conductive wall switching in TiO_2 and TiO_2:Co self-organized nanotube arrays. J. Alloys Compd. **825**, 154006 (2020).

15. Ali T., Ahmed A., Siddique M.N., Alam U., Muneer M. and Tripathi P., Influence of Mg^{2+} ion on the optical and magnetic properties of TiO_2 nanostructures: A key role of oxygen vacancy. Optik − International Journal for Light and Electron Optics **223**, 165340 (2020).

16. Tseng, L.-T., Luo X., Tan T.T., Li S. and Yi J., Doping concentration dependence of microstructure and magnetic behaviours in Co-doped TiO_2 nanorods. Nanoscale Res. Lett. **9**, 673 (2014).

17. Kumar A., Hussain I., Kumar S. and Koo B.H., Structural, optical properties and the origin of spin functionality in the Co modified TiO_2 nanoparticles. Vacuum **183**, 109870 (2021).

18. Senthil S., Raman D.N. and Sundaramoorthy A., Study of the magnetic properties of Mn-doped

iron titanate nanoparticles fabricated using natural mineral. Micro Nano Lett. **15**, 1–6 (2020).

19. Abo-Naf S.M. and Marzouk M.A., Tunable blue and green emissions of sol–gel synthesized transparent nano-willemite codoped with nano-pyroxmangite and dysprosium. Nano-Struct. Nano-Objects **26**, 100685 (2021).

20. Djerdj I. and Tonejc A.M., Structural investigations of nanocrystalline TiO_2 samples. J. Alloys Compd. **413**, 159–174 (2006).

21. Arunmetha S., Dhineshbabu N.R., Kumar A. and Jayavel R., Preparation of sulfur doped TiO_2 nanoparticles from rutile sand and their performance testing in hybrid solar cells. J. Mater. Sci. Mater. Electron. **32**, 28382–28393 (2021).

22. Chouhan L., Narzary R., Dey B.; Panda S.K., Manglam M.K., Roy L., Brahma R., Mondal A., Kar M., Ravi S. and Srivastava S. K., Tailoring room temperature d^0 ferromagnetism, dielectric, optical, and transport properties in Ag-doped rutile TiO_2 compounds for spintronics applications. J. Mater. Sci. Mater. Electron. **32**, 28163–28175 (2021).

23. Radhamani A.V., Surendra M.K. and Rao M.S.R., Tailoring the supercapacitance of Mn_2O_3 nanofibers by nanocompositing with spinel-$ZnMn_2O_4$. Mater. Des. **139**, 162–171 (2018).

24. Ahmed S.A., Influence of Mn doping on structural and magnetic properties of $Ti_{1-x}Mn_xO_2$. J. Mater. Sci. Mater. Electron. **27**, 7589–7594 (2016).

25. Prajapati B., Roy S., Sharma S., Joshi A.G.S., Chatterjee and Ghosh A.K., Bandgap engineering and signature of ferromagnetism in $Ti_{1-x}Mn_xO_2$ diluted magnetic semiconductor nanoparticles: A valence band study. Phys. Status Solidi B. **256**, 1800262(2019).

26. Sharma S., Chaudhary S., Kashyap S.C. and Malik V.K., DC magnetization investigations in $Ti_{1-x}Mn_xO_2$ nanocrystalline powder. J. Alloys Compd. **509**, 7434–7438 (2011).

27. Sellers M.C.K. and Seebauer E.G., Room temperature ferromagnetism in Mn-doped TiO_2 nanopillar matrices. Mater. Lett. **114**, 44–47 (2014).

28. Choudhury B. and Choudhury A., Oxygen vacancy and dopant concentration dependent magnetic properties of Mn doped TiO_2 nanoparticles. Curr. Appl. Phys. **13**, 1025–1031 (2013).

29. Choudhury B., Paul S., Ahmed G.A. and Choudhury A., Adverse effect of Mn doping on the magnetic ordering in Mn doped TiO_2 nanoparticles. Mater. Res. Express **2**, 096104 (2015).

30. Khan A.A., Tahir M. and Zakaria Z.Y., Synergistic effect of anatase/rutile TiO_2 with exfoliated $Ti_3C_2T_R$ MXene multilayers composite for enhanced CO_2 photoreduction via dry and bi-reforming of methane under UV–visible light. J. Environ. Chem. Eng. **9**, 105244 (2021).

31. Liu K., Wang G., Meng M., Chen S., Li J., Sun X., Yuan H., Sun L. and Qin N., TiO_2 nanotube photonic crystal fabricated by two-step anodization method for enhanced photoelectrochemical water splitting. Mater. Lett. **207**, 96–99 (2017).

32. Cuauhtémoc-López I., Jiménez-Vázquez A., Estudillo-Wong L.A., Torres-Torres G., Pérez-Vidal H., Barrera-Salgado M., López-González R. and Cruz-Romero D.D., Naphthalene hydrogenation using Rh/Fe_2O_3-TiO_2 magnetic catalysts. Catal. Today 360, 176–184 (2021).

33. Bharati B., Mishra N.C., Sinha A.S.K. and Rath C., Unusual structural transformation and photocatalytic activity of Mn doped TiO_2 nanoparticles under sunlight. Mater. Res. Bull. 123, 110710 (2020).

34. Dias J.A., Freire A.L.F., Girotto I., Roveri C.D., Mastelaro V.R., Paris E.C. and Giraldi T. R., Phase evolution and optical properties of nanometric Mn-doped TiO_2 pigments. Mater. Today Commun. **27**, 102295 (2021).

35. Zhou Z., Ding C., Peng W., Li Y., Zhang F. and Fan X., One-step fabrication of two-dimensional hierarchical Mn_2O_3@graphene composite as high-performance anode materials for lithium ion batteries. J. Mater. Sci. Technol. **80**, 13–19 (2021).

36. Azab A.A., Ateia E.E., Esmail S.A., Comparative study on the physical properties of transition metal-doped (Co, Ni, Fe, and Mn) ZnO nanoparticles. Appl. Phys. A **124**, 469 (2018).

37. Azab A.A., Esmail A., Abdelamksoud M.K., Studying the effect of cobalt doping on optical and magnetic properties of zinc oxide nanoparticles. Silicon **11**, 165–174 (2019).

38. Bousiakou L.G., Dobson P.J., Jurkin T., Marić I., Aldossary O. and Ivanda M., Optical, structural and semiconducting properties of Mn doped TiO_2 nanoparticles for cosmetic applications. J. King Saud Uni. Sci. **34**, 101818 (2022).

39. Caligulu U., Darcan N. and Kejanli H., Surface morphology and optical properties of Ca and Mn doped TiO_2 nano-structured thin films. Eng. Sci. Technol. Int. J. **24**, 1292–1300 (2021).
40. Akshay V.R., Arun B., Mukesh M., Chanda A. and Vasundhara M., Tailoring the NIR range optical absorption, band-gap narrowing and ferromagnetic response in defect modulated TiO_2 nanocrystals by varying the annealing conditions. Vacuum **184**, 109955 (2021).
41. ElBatal F.H., Azooz M. A., Hamdy Y.M., Ezz ElDin F.M., Abo-Naf S. M., and ElBatal H. A., Optical, photoluminescence, and E.S.R spectral analysis of manganese ions in phosphate glasses melted under various conditions and impact of gamma irradiation. J. Mater. Sci. Mater. Electron. **33**, 5477–5488 (2022).
42. Yu Y., Liu Z., Dai N., Sheng Y., Luan H., Peng J., Jiang Z., Li H., Li J. and Yang L., Ce-Tb-Mn co-doped white light emitting glasses suitable for long-wavelength UV excitation. Opt. Express **19**, 19473–19479 (2011).
43. Morad I., Liu X. and Qiu J., Surface crystallized Mn-doped glass-ceramics for tunable luminescence. J. Am. Ceram. Soc. **102**, 5843–5852 (2019).
44. Czaja M., Lisiecki R., Chrobak A., Sitko R. and Mazurak Z. The absorption- and luminescence spectra of Mn^{3+} in beryl and vesuvianite. Phys. Chem. Miner. **45**, 475–488 (2018).
45. Bhandarkar S.A., Prathvi, Kompa A., Murari M.S., Kekuda D. and Mohan R. K., Investigation of structural and optical properties of spin coated TiO_2:Mn thin films. Opt. Mater. **118**, 111254 (2021).
46. Pan L., Xu G., Guo T., Zhang B., Xiang, S., Fang G. and Li J., Study on thermochromic-emissivity performance of Mn doped TiO_2 under temperature fluctuations. Infrared Phys. Technol. **105**, 103192 (2020).
47. Ravi S. and Shashikanth F.W., Magnetic properties of Mo-doped TiO_2 nanoparticles: A candidate for dilute magnetic semiconductors. Mater. Lett. **264**, 127331 (2020).
48. Waseem S., Anjum S., Zeeshan T. and Shah I., Effects of Cr-doping on structural, morphological, magnetic, optical and electrical properties of $Ti_{0.9}Fe_{0.1-x}O_2$ thin films. Optik - International Journal for Light and Electron Optics **212**, 164630 (2020).
49. Hameed T.A., Azab A.A., Ibrahim R.S., Rady K.E., Optimization, structural, optical and magnetic properties of TiO_2/ $CoFe_2O_4$ nanocomposites. Ceram. Int. **48**, 20418–20425 (2022).
50. Zhang H., Xu Y., Ouyang X. and Ni Y., Interplay of dopants and defects in magnetic evolution of La and Fe co-doped TiO_2 nanoparticle. J. Sol-Gel Sci. Technol. **83**, 365–374 (2017).
51. Zhang H., Xu Y., Yang W. and Lin R., Structural and magnetic evolution of Fe-doped TiO_2 nanoparticles synthesized by sol-gel method. J. Electroceram. **38**, 104–110 (2017).
52. Vranješ M., Jakovljević J.K., Milošević M., Ćirić-Marjanović G., Stoiljković M., Konstantinović Z., Pavlović V., Milivojević D. and Šaponjić Z., Hydrothermal synthesis of Mn^{2+} doped titanate nanotubes: Investigation of their structure and room temperature ferromagnetic behavior. Solid State Sci. **94**, 155–161 (2019).
53. Kim K.J., Park Y.R., Lee J.H., Choi S.-L., Lee H.J., Kim C.S. and Park J.Y., Room-temperature ferromagnetic properties in Mn-doped rutile $TiO_{2-\delta}$ thin films. J. Magn. Magn. Mater. **316**, e215–e218 (2007).